"Doughnut" nuclear shapes in head-on heavy ion collisions

Konstantin Cherevko,[1,2,3,*] Leonid Bulavin,[3] Jun Su,[1,2] Vladimir Sysoev,[3] and Feng-Shou Zhang[1,2,4,†]

[1]*Key Laboratory of Beam Technology and Material Modification of Ministry of Education, College of Nuclear Science and Technology, Beijing Normal University, Beijing 100875, China*

[2]*Beijing Radiation Center, Beijing 100875, China*

[3]*Physics Department, Taras Shevchenko National University of Kyiv, 4 Glushkova Avenue, Kyiv 03022, Ukraine*

[4]*Center of Theoretical Nuclear Physics, National Laboratory of Heavy Ion Accelerator of Lanzhou, Lanzhou 730000, China*

(Received 13 June 2013; revised manuscript received 22 November 2013; published 30 January 2014)

Based on the hydrodynamic approach, the formation of exotic structures in head-on heavy ion collisions at 60 MeV/nucleon is explained. The physical explanation of the different structures' formation with dependence on the incompressibility coefficient is suggested. Within the developed approach the Rayleigh-Plateau mechanism is confirmed to be the origin of the fragments in the case of "stiff" equation of state of nuclear matter (with an incompressibility of 380 MeV). The cold breakdown of the system is suggested to be caused by the presence of the Coulomb force. The obtained results are compared with the existing Boltzmann-like theory calculations and the experimental data for the "doughnut" -like geometries.

DOI: 10.1103/PhysRevC.89.014618 PACS number(s): 25.70.−z, 24.10.Nz

I. INTRODUCTION

During recent decades in a number of works the possibility of toroidal and bubble structure formation in head-on heavy ion collisions (HIC) was studied extensively with the help of microscopic transport models [1,2]. Such types of structures are somewhat similar to those studied theoretically from another approach [3]. For some time experimental results were not able to confirm the occurrence of the predicted geometries [4], but later on the signatures of "doughnut"-like structures with production of similar size intermediate mass fragments (IMF) were observed in central HIC [5] and again confirmed by transport models [6]. Unfortunately the transport theory calculations used for the phenomena in focus are not able to give reliable information on multiparticle observables at the late stages of the process, due to the fact that they do not include multiparticle correlations and fluctuations [2]. Therefore, up to now the model of the phenomena describing in detail the underlying physical mechanism of the possible exotic structures formation in HIC has been somehow lacking. At the same time the reliable physical model of the process may be helpful in extending the progress in the studies of the nuclear equation of state (EOS) that is one of the fundamental goals in nuclear physics and nuclear astrophysics [7].

In this paper we report an attempt to study the problem from the different sides and dwell on the hydrodynamic description of head-on HIC. Among the reasons for such a decision are the successful implementation of hydrodynamic and thermodynamic methods for the description of nuclear systems [8–12], good correspondence between hydrodynamics and transport theories [13], and the similarity of the qualitative pictures observed in head-on HIC and in the case of high speed ordinary droplet collisions [14–16]. For the latter, in a certain energy range the formation of the doughnut-like structures with the following fragmentation into several secondary drops of approximately equal masses is observed [17], which has much in common with the nuclear case [2].

To set the stage, we recall that hydrodynamic description of nuclear matter dates back to the 1980s [8]. Now, the hydrodynamic description is widely used for high energy HIC. In some pioneer works [9] the possibility of using a hydrodynamic description for the lower energy limit was confirmed based on the analysis of the nucleon mean free path, which was defined as $\lambda = 1.4\frac{\rho_0}{\rho}$ fm. Later on quite a lot of works addressed the problem of the nucleon mean free path and in-medium nucleon cross-section evaluation, with Pauli blocking being considered [18]. Still, the results found in some more recent publications [6] with parameterized in-medium nucleon-nucleon cross sections from the Dirac-Brueckner approach based on the Bonn-A potential give the values $\lambda \sim 1.4$ fm and $\lambda \sim 1.3$ fm for $\rho/\rho_0 = 1$ and $\rho/\rho_0 = 1.5$ respectively at $E = 50$ MeV/nucleon. Those results confirm well the argumentation of Ref. [9]. Despite that, the hydrodynamic description of HIC at intermediate and low energies has been the subject of only few theoretical studies [19]. By contrast, the behavior of colliding ordinary liquid droplets in a wide range of impact velocities and its dependence on the compressibility, surface tension, and viscosity and has been extensively studied in the literature [20–22]. Those studies resulted in changes of the qualitative picture of the process due to a better understanding of the underlying physics.

All this suggests using the achievements of the ordinary liquid droplet collision theory to revive the hydrodynamic approach for the description of head-on HIC at intermediate energies $E \sim 60$ MeV/nucleon. Therefore, our focus here is on such a description with the shockwave mechanism [1,23] taken into account.

II. THEORETICAL MODEL

We consider the system of two identical heavy nuclei (e.g., ^{93}Nb + ^{93}Nb) involved in a head-on collision. The symmetry of the system allows the simplification of the model by

*konstantin.cherevko@gmail.com

†Corresponding author: fszhang@bnu.edu.cn

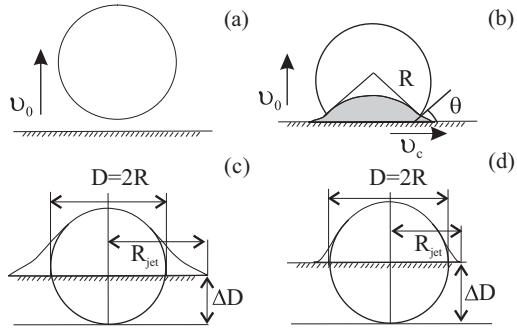

FIG. 1. Different stages of the system evolution: (a) symmetry plane impacting the nucleus; (b) lateral jetting when the shockwave velocity becomes equal to the contact edge velocity. The compressed zone is shown in grey. (c) System geometry for the case of "stiff" EOS ($K = 380$ MeV). (d) System geometry for the case of "soft" EOS ($K = 200$ MeV).

changing to the collision of a spherical nucleus of radius R and density ρ_0 with a rigid wall that moves towards it with the velocity υ_0 [Fig. 1(a)]. The slip boundary condition is applied on the wall surface to account for the difference in a viscous behavior.

The first step towards a better understanding of the process is an analysis of the possible sources of different system geometries. In Ref. [1] it has been argued that the system evolves from one geometry to the other as time passes. At the same time from the figures presented in Ref. [2] one can see that for the cases of "soft" and "stiff" EOS the topology of the system is different already at $t \sim 40$ fm/c and does not change after that. As one expects intuitively, within the hydrodynamic approach the main difference between the EOS comes from the elastic properties of the matter. It is obvious that those properties can make a notable difference in a system behavior when the compression rate is high and some shockwaves are formed in the system. Therefore, the topology is probably defined during the first violent stage of the collision and remains unchanged until system breakdown.

Recent theoretical and experimental results for liquid droplet collisions [24–26] together with the Boltzmann-Uehling-Uhlenbeck (BUU) [2] model and nuclear fluid dynamics (NFD) [23] results for HIC point towards four distinct stages of the collision (Fig. 1). Among them are a violent stage at the beginning of the process when the highly compressed zone is formed, and a second stage that is characterized by lateral jetting and lasts until the shockwave from the collision plane reaches the boundary of the nucleus. During those two stages the final topology of the system is fully defined. At the later times the system goes through a third stage corresponding to the expansion process, and finally comes to the last stage when the fragmentation takes place. We try to develop a self-consistent model that accounts for the different physics at each stage of the processes and in which the quantitative and qualitative characteristics of the system at the end of each stage work as the initial conditions for the next one.

A. Initial violent stage

To describe the initial moments of the impact of compressible nucleus with the wall it is possible to apply the high

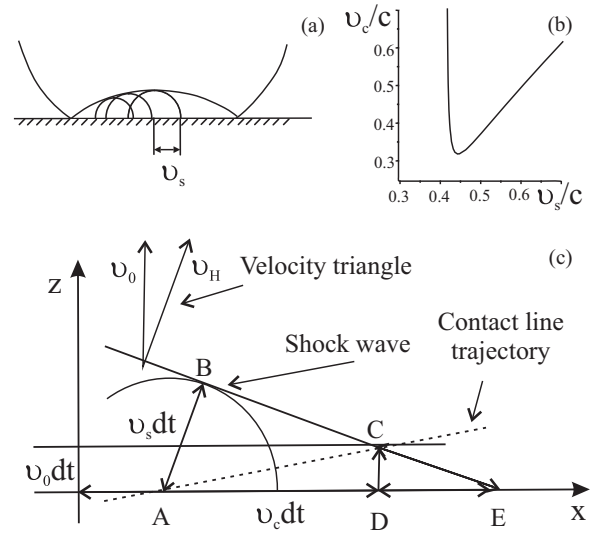

FIG. 2. Initial stage of the nucleus collision with the rigid wall. (a) Huygens construction shows the shock envelope in the colliding system. (b) Contact edge velocity υ_c dependence on the shockwave velocity υ_s in the compressed part. (c) Geometrical construction of the shock profile in the reference system moving together with the contact point [30].

speed compressible droplet impact shockwave model from Refs. [27,28]. Within this model, according to the Huygens principle the expanding nucleus edge emits wavelets that propagate with shockwave velocity υ_s in all the directions and are the only source of the surface distortion [Fig. 2(a)]. This leads to the development of strong compression with maximum density $\rho_{\max}$ at the contact line. The shape of the system is defined by the geometrical overlap of colliding nucleons as the shockwave velocity υ_s is smaller than the contact line velocity υ_c, and hence it is not possible for matter to leave the geometrically defined region. Such a picture has much in common with the one observed in the NFD calculations that justifies us in using the above model.

The general analytical solution for the initial stage was obtained in Ref. [30] for ordinary liquids. Within this approach the relation between the contact line velocity υ_c, shockwave velocity υ_s, and particle velocity jump on the discontinuity υ_H is found from the geometrical relations [similarity of the triangles ABE, CDE, and velocity triangle in Fig. 2(c)]. Starting from the simple geometrical relation:

$$\frac{\upsilon_c dt + DE}{\upsilon_s dt} = \frac{\sqrt{(\upsilon_0 dt)^2 + DE^2}}{\upsilon_0 dt}, \tag{1}$$

with dt being the time needed for the contact point to move from A to C, and employing the well known consequence of the Euler equation that υ_H is normal to the shockwave together with the similarity of triangle CED and the velocity triangle yields

$$\frac{\upsilon_H}{\upsilon_0} = \frac{CE}{DE} = \frac{CE\,dt}{DE\,dt}. \tag{2}$$

From Eq. (2) and the equation coming from the similarity of the triangle AEB and velocity triangle,

$$\frac{CE}{dt} = \upsilon_0 \frac{\upsilon_c + \frac{DE}{dt}}{\upsilon_s}, \tag{3}$$

one may obtain the relation between the contact line velocity υ_c, sound velocity υ_s, and particle velocity jump υ_H:

$$\upsilon_H = \frac{{\upsilon_0}^2}{\upsilon_s}\left(\upsilon_c \frac{dt}{DE} + 1\right). \tag{4}$$

Finally, after substitution of $\frac{DE}{dt}$ from Eq. (1), Eq. (4) becomes

$$\upsilon_H(\upsilon_s) = \upsilon_0 \frac{\left(\upsilon_s + \upsilon_0\sqrt{1 - \frac{{\upsilon_s}^2 - {\upsilon_0}^2}{{\upsilon_c}^2}}\right)}{\left(\upsilon_0 + \upsilon_s\sqrt{1 - \frac{{\upsilon_s}^2 - {\upsilon_0}^2}{{\upsilon_c}^2}}\right)}. \tag{5}$$

Equation (5) contains three unknowns and, therefore, in order to use it an additional piece of information for the relation between υ_s and υ_H is needed. It should be noted that the shockwave velocity is not constant during the process and is EOS dependent. In Ref. [30] it was taken in the form of the linear dependence of the shockwave velocity on the particle velocity $\upsilon_s = \upsilon_{s0} + k\upsilon_H$ based on the ordinary liquid EOS. To adopt the approach of [30] for our case it is necessary to analyze the relation between the υ_s and υ_H based on the EOS of nuclear matter.

The linear dependence of υ_s on υ_H used by [30] is the particular case of the general expansion of υ_s into the McLaurin series [31]

$$\upsilon_s = \upsilon_{s0} + k\upsilon_H + k_1{\upsilon_H}^2 + k_2{\upsilon_H}^3 + \cdots, \tag{6}$$

were υ_{s0} is the ambient sound velocity. To evaluate the coefficients $k, k_1, \ldots$ of the expansion for the case of nuclear matter we start from the Rankine-Hugoniot equations in the reference frame where the nucleons before the shock front have zero velocity $\upsilon = 0$ as in our model, the nucleus is at rest, and the wall is moving towards them. In that case the equations defining pressure $P_H = P' - P$ and velocity $\upsilon_H = \upsilon' - \upsilon \equiv \upsilon'$ jumps at the discontinuity have the form

$$\rho_0\upsilon_s = \rho(\upsilon_s - \upsilon_H), \quad P_H = m_p\rho_0\upsilon_s\upsilon_H, \tag{7}$$

were primes denote the values after the shock front. In this paper we limit ourselves to the case when the temperature changes are not included in the analysis and we do not use the third Rankine-Hugoniot equation for the energy conservation. Therefore, to have a closed system we use the EOS of nuclear matter in a form [7] where only compression energy per particle is included but not the thermal one:

$$U(\rho) = \alpha\left(\frac{\rho}{\rho_0}\right) + \beta\left(\frac{\rho}{\rho_0}\right)^{\gamma}, \tag{8}$$

$$P = \rho^2\frac{\partial E_B}{\partial\rho}, \quad E_B = \frac{3}{5}E_F + \frac{1}{\rho}\int U(\rho)d\rho, \tag{9}$$

where U is the single-particle potential, E_B is the binding energy per particle, and E_F is the Fermi energy. Parameters α, β, and γ are chosen to give the different values of incompressibility K for the saturation density ρ_0 (Table I).

TABLE I. Parameters of the EOS of nuclear matter [29].

	Soft EOS	Stiff EOS
α (MeV)	−356	−124
β (MeV)	303	70.5
γ	7/6	2
K (MeV)	200	380

From Eqs. (7), (8), and (9) one can get the expression for the shockwave velocity in the form

$${\upsilon_s}^2 = \frac{1}{m}\frac{\upsilon_s}{\upsilon_H}\left(\frac{h^2}{5m}\frac{\left(\frac{3\rho_0}{4g\pi}\right)^{\frac{2}{3}}}{\left(1 - \frac{\upsilon_H}{\upsilon_s}\right)^{\frac{5}{3}}} + \frac{\alpha}{2\left(1 - \frac{\upsilon_H}{\upsilon_s}\right)^2} + \frac{\beta\gamma}{(\gamma+1)\left(1 - \frac{\upsilon_H}{\upsilon_s}\right)^{\gamma+1}} - \frac{P_0}{\rho_0}\right), \tag{10}$$

where $P_0 = 0$ is the pressure of nuclear matter at equilibrium. Eq. (10) can be expanded into series:

$${\upsilon_s}^2 = a_0 + a_1\left(\frac{\upsilon_H}{\upsilon_s}\right) + a_2\left(\frac{\upsilon_H}{\upsilon_s}\right)^2 + \cdots. \tag{11}$$

Inserting (6) into (11) yields a system of equations to deduce the coefficients in the expansion (6). The performed analysis of the series has shown that the contribution of the cubic term is negligible. Therefore, in this work we substantially followed the geometrical approach from Ref. [30], but adopted for the shockwave velocity

$$\upsilon_s = \upsilon_{s0} + k\upsilon_H + k_1{\upsilon_H}^2. \tag{12}$$

Coefficients υ_{s0}, k, and k_1 calculated for nuclear matter are given in Table II. Finally, solving Eq. (5) for υ_c subject to (12) leads to

$$\upsilon_c(\upsilon_s) = \frac{\upsilon_s(\sqrt{k^2 - 4k_1(\upsilon_{s0} - \upsilon_s)} - k) - 2k_1{\upsilon_0}^2}{\sqrt{(\sqrt{k^2 - 4k_1(\upsilon_{s0} - \upsilon_s)} - k)^2 - 4k_1^2{\upsilon_0}^2}}. \tag{13}$$

The compression stage lasts for τ_1 until the moment when the contact line velocity becomes equal to the shockwave velocity $\upsilon_s^{\max}$. After that lateral jetting in a direction perpendicular to the beam axis occurs and the shape of the system is changing [Fig. 1(b)]. That picture can be confirmed by the anomalous behavior of the contact line velocity υ_c dependence on the shockwave velocity shown in Fig. 2(b). The observed unphysical growth of υ_c after the shockwave velocity reaches

TABLE II. Coefficients of the McLaurin series expansion for the sound velocity in the cases of soft ($K = 200$ MeV) and stiff ($K = 380$ MeV) EOS.

	Soft EOS	Stiff EOS
υ_{s0} (c)	0.15	0.21
k	1.32	1.54
k_1 ($1/c$)	0.16	0.21

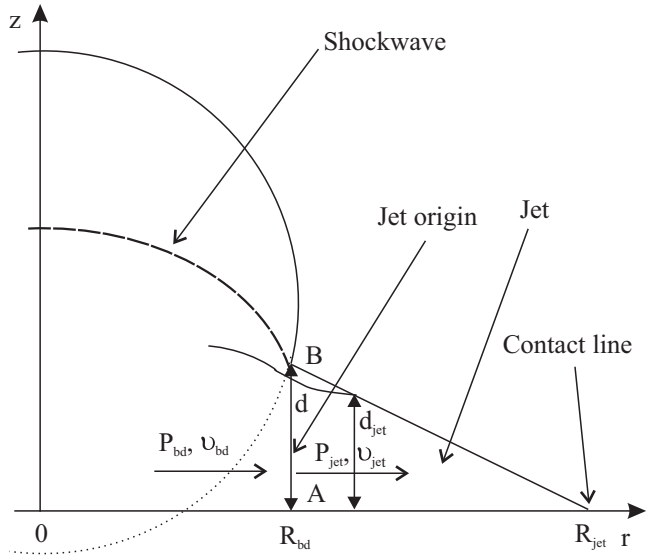

FIG. 3. Schematic picture of the jetting stage.

the value $\upsilon_s^{\max}$ suggests that the acquired physics with a single shockwave attached to the contact point is not valid thereafter.

B. Jetting stage

The jetting stage is characterized by the lateral jetting that emerges from the compressed zone and by changes of the geometry of the system [Figs. 1(b), 1(c), and 1(d)]. To have an approximate quantitative description we introduce a model of the outflow through the hole [25,32,33] formed by the wall and the shockwave that travels along the free surface of the nucleus (AB in Fig. 3). The governing equation for this stage is the Bernoulli equation

$$\frac{P_{bd}}{m_p\rho_{bd}}+\frac{{\upsilon_{bd}}^2}{2}=\frac{P_{\rm jet}}{m_p\rho_{\rm jet}}+\frac{{\upsilon_{\rm jet}}^2}{2}+\zeta\frac{{\upsilon_{\rm jet}}^2}{2}+\frac{2\sigma}{m_p\rho_{\rm jet}R_{\rm jet}}, \tag{14}$$

where P, ρ, and υ are the pressure, density and particle velocity respectively, and σ is the surface tension coefficient. Subscripts "bd" and "jet" are for the values inside the nucleus and in the jet respectively (Fig. 3). Function $\zeta\frac{{\upsilon_{\rm jet}}^2}{2}$ is the loss function in a Darcy-Weisbach [32] form and the term $\frac{2\sigma}{\rho_{\rm jet}R_{\rm jet}}$ accounts for the non-negligible surface pressure that is important for nuclear matter. In order to justify using the Bernoulli equation for incompressible liquids (14) in the studied case, we treat the system in the approximation of equal densities before and after the hole $\rho_{bd}=\rho_{\rm jet}$ that works well for compressible ordinary liquids [25,34]. Solving Eq. (14) for the particle velocity in the jet gives

$$\upsilon_{\rm jet}=\sqrt{\frac{1}{1+\zeta}}\sqrt{\frac{2(P_{bd}-P_{\rm jet})}{m_p\rho_{bd}}+{\upsilon_{bd}}^2-\frac{2\sigma}{m_p\rho_{bd}R_{\rm jet}}}, \tag{15}$$

were the coefficient $\phi=\sqrt{\frac{1}{1+\zeta}}$ is the velocity coefficient that accounts for the head loss due to the compression of the jet. The corresponding volumetric flow rate Q is [32]

$$\begin{aligned}Q&=2\pi R_{bd}d\xi\upsilon_{\rm jet}\\&=2\pi R_{bd}d\xi\phi\sqrt{\frac{2(P_{bd}-P_{\rm jet})}{m_p\rho_{bd}}+{\upsilon_{bd}}^2-\frac{2\sigma}{m_p\rho_{bd}R_{\rm jet}}},\end{aligned} \tag{16}$$

where R_{bd} and d are the radius and the height of the hole and $\xi=\frac{d_{\rm jet}}{d}<1$ is the compression coefficient equal to the relation of the jet cross section and the hole cross section. At this point we account for the temporal evolution of the pressure $P=P(t)$, density $\rho=\rho(t)$, the size of the hole $d=d(t)$, and particle velocity $\upsilon_{bd}=\upsilon_{bd}(t)$. In this paper we assume that the thickness of the jet behaves like $h_{\rm jet}(r,t)=\frac{g(t)}{r}$, which with the time-dependent boundary condition $h_{\rm jet}(R_{bd},t)=d(t)$ gives

$$h_{\rm jet}(r,t)=\frac{d(t)R_{bd}(t)}{r}. \tag{17}$$

Such an approximation corresponds well to the existing studies of the impacts of compressible droplets of ordinary liquids [25,34] and it can give the correct results by an order of magnitude. The results for the different behaviors of the thickness can be found elsewhere [35]. In the two-dimensional model, representing a thin parallel slice taken vertically through the impacting nucleus (which corresponds to the picture in Fig. 3) it is possible to change from the volumetric flow rate to its square. Thus, changing from cylindrical geometry with z axis to the infinite layer geometry from Eqs. (16) and (17), it is possible to define the system geometry changes $R_{\rm jet}(t)$ [Figs. 1(c) and 1(d)] in the form

$$\begin{aligned}&\int_{R_{bd}(\tau)}^{R_{\rm jet}(\tau)}\frac{R_{bd}(\tau)d(\tau)}{r}dr\\&\quad=\int_{\tau_1}^{\tau}d(t)\xi\phi\sqrt{\frac{2P_{bd}(t)}{m_p\rho_{bd}(t)}+{\upsilon_{bd}(t)}^2-\frac{2\sigma}{m_p\rho_{bd}R_{\rm jet}}}dt,\end{aligned} \tag{18}$$

where we account for the condition $P_{\rm jet}=0$. It is important to mention here that the pressure $P_{bd}(t)$ and particle velocity $\upsilon_{bd}(t)$ are not constant along the hole cross section. The shockwave pressure P_H and velocity are high at the intersection of the shockwave with the free surface of the droplet (point B in Fig. 3) and decrease when approaching the contact line in the origin of the jet (point A in Fig. 3) [36]. Accounting for that distribution can allow defining the exact shape and volume of the jet. In our model the shape of the jet is assumed to have the form (17). Therefore, to keep the governing equations as simple as possible to allow for an analytical description, we use in all the subsequent equations the averaged values of $P_{bd}(t)$ and $\upsilon_{bd}(t)$ over the jet cross section that give the correct volumetric flow rate at each moment of time. The above equation (18) must be solved with the initial conditions that come from the initial violent stage:

$$P_{bd}(\tau_1)=P_1(\tau_1),\quad \upsilon_{bd}(\tau_1)={\upsilon_1}^{\rm rad}(\tau_1), \tag{19}$$

where ${\upsilon_1}^{\rm rad}(\tau_1)$ and $P_1(\tau_1)$ are the radial particle velocity and pressure at the contact line at the beginning of the jetting stage (at τ_1 points A and B in Fig. 3 coincide).

The velocity ϕ and compression ξ coefficients in (18) are tabulated in the hydraulics reference books for the different hole parameters [32]. During the studied process their product varies from $\xi\phi = 0.45$ for the "conical nozzle" to $\xi\phi \sim 1$ for the "big hole in a thin wall." In this paper, to keep the picture clear we adopt it to be constant with the average value $\xi\phi = 0.64$ that gives the correct result for the overall volume accumulated in the jet during the stage.

Evaluating the size of the jet from Eq. (18) leads to two different shapes depending on the stiffness of the EOS, as can be seen from Figs. 1(c) and 1(d). The description of the next stages would be different for the soft ($K = 200$ MeV) and stiff ($K = 380$ MeV) EOS as the qualitative physical pictures for that cases are not the same [37]. Hereafter we will focus on the toroidal structures as their occurrence have some experimental confirmation [5].

C. Expansion stage

Next, from the analysis of the existing experimental [38] and computer simulation [24,39] data for liquid droplet collisions it is possible to assume that, within the hydrodynamic approach, at τ_2 when the shockwave reaches the top of the nucleus the inertia-dominated transformation of a "pancake"-like nucleus into an expanding lamella is observed. At this stage the pressure in the flow decreases very quickly and becomes insignificant as a driving force for the flow [24,40]. Due to the existence of the surface forces the expanding lamella of radius R_l will be surrounded by a thicker rim with radius $R_{\rm rim}$ that during the evolution will accumulate most of the matter [Fig. 4(a)]. From hereafter we change back from the model with the wall impacting the nucleus to the two colliding nucleus. It is important to do this in the description of the expansion stage because at that time the balance between the inertia and capillary forces comes into play. Correct treatment of this interplay requires realistic estimates for the balance between the overall volume of the system and the volume accumulated in the rim that is dependent on the rim geometry.

In order to obtain the qualitative picture of the phenomena, in this work we assume an inviscid case and start from Euler equations in a slender slope approximation $\frac{\partial h}{\partial r} \ll 1$:

$$\rho\left(\frac{\partial \upsilon}{\partial t} + \upsilon\frac{\partial \upsilon}{\partial r}\right) = -\frac{\partial p}{\partial r}, \quad r\frac{\partial h}{dt} + \frac{\partial(r\upsilon h)}{\partial r} = 0, \tag{20}$$

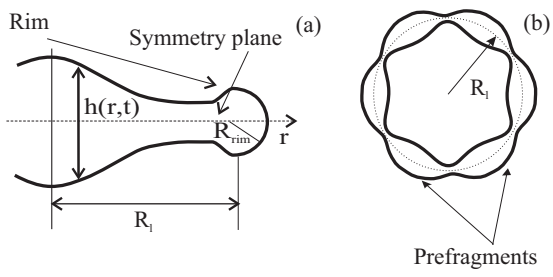

FIG. 4. (a) Rim formation at the edge of the expanding lamella. (b) Schematic front view picture of the "varicose" deformation of the rim.

where r is the radial coordinate and h is the thickness of the lamella. Thus, we assume that compressibility of the matter does not play an important role during this stage of the collision.

In our studies we substantially follow the description from [41] and search for the solution assuming the lamella thickness to behave like

$$h(r,t) = \frac{f(t)}{r}, \tag{21}$$

where $f(t)$ is some unknown function of time. Such a shape of the lamella is confirmed by studies devoted to a continuous liquid jet impacting a solid target [42] and is in agreement with the shape of the jet adopted in this work [Eq. (17)] for the jetting stage. Equation (21), owing to the second equation of (20) with the lamella attached to the central point, that is $\upsilon(0,t) = 0$, implies

$$\upsilon(r,t) = -\frac{\frac{df(t)}{dt}}{f(t)}r. \tag{22}$$

The solution for $f(t)$ is constrained by two additional conditions which express that the radially expanding nucleons are arrested at some distance from the impact point $R_l(t)$ by capillary confinement and that they feed the lamella rim at which they progressively all collect. First is the volume balance in the system given by

$$\int_0^{R_l} 2\pi r h(r,\tau)dr = 2\Omega - \int_{\tau_2}^{\tau} 2\pi R_l(t)\left(\upsilon(R_l,t) - \frac{dR_l}{dt}\right) \times h(R_l,t)dt, \tag{23}$$

where $\Omega = \frac{4}{3}\pi R^3$ is the initial volume of the nucleus. The left-hand side shows the volume of the lamella when the second term on the right-hand side gives the volume of the rim at time τ. The second comes from momentum conservation at the rim of mass $M_{\rm rim}(t)$. One has a kind of a propulsion movement; therefore, the starting point is Meschersky's equation in the form

$$M_{\rm rim}(t)\frac{d^2R_l(t)}{dt^2} = \left(\upsilon(t) - \frac{dR_l(t)}{dt}\right)\frac{dM_{\rm rim}(t)}{dt} + F, \tag{24}$$

where $F = -4\sigma\pi R_l$ is the external force acting on the rim. Introducing the mass of the rim per unit arclength $m(t)$ and accounting for the mass change $\frac{dM_{\rm rim}(t)}{dt} = m_p\rho h(R_l,t)2\pi R_l(t)(\upsilon(R_l,t) - \frac{dR_l(t)}{dt})$, one obtains in axisymmetric coordinates

$$\frac{d}{dt}\left(mR_l\frac{dR_l}{dt}\right) = m_p\rho\upsilon(R_l,t)R_l(t)h(R_l,t) \times \left(\upsilon(R_l,t) - \frac{dR_l(t)}{dt}\right) - 2\sigma R_l. \tag{25}$$

For the considered phenomena for a broad range of impact velocities and surface tension coefficients $\frac{d(mR)}{dt}/(mR) \gg \frac{d^2R}{dt^2}/\frac{dR}{dt}$ [41], which allows neglecting the term $m\frac{d^2R}{dt^2}$. Thus, (25) reduces to

$$m_p\rho h(R_l,t)\left(\upsilon(R_l,t) - \frac{dR_l(t)}{dt}\right)^2 = 2\sigma. \tag{26}$$

Equations (23) and (26) when solved using (21) and (22) for $h(r,t)$ and $\upsilon(r,t)$ give

$$f(t)R_l(t) = \frac{\sigma}{2m_p\rho}((B-t)^2 + A),$$
$$B = \tau_2 + \sqrt{\frac{2m_p\rho}{\sigma}}\sqrt{\frac{\Omega}{\pi}} \quad (27)$$
$$A = \frac{2m_p\rho}{\sigma}\left(2R_{bd}(\tau_2)d(\tau_2)R_{\rm jet} - \frac{\Omega}{\pi}\right),$$

where the initial conditions $f(\tau_2) = 2R_{bd}(\tau_2)d(\tau_2)$ and $R_l(\tau_2) = R_{\rm jet}$ come from the jetting stage. The momentum equation [the first of Eqs. (20)] when integrated from $r = 0$ to $r = R_l(t)$ gives

$$\frac{m_p\rho {R_l}^2}{2}\left(-\frac{\frac{d^2f(t)}{dt^2}}{f(t)} + 2\left(\frac{\frac{df(t)}{dt}}{f(t)}\right)^2\right) = 0, \quad (28)$$

where we assume the absence of the pressure gradient along r during the late stages of the collision. There are several reasons for that. First, we disregard any interaction with the ambient medium. Second, we use an inviscid approximation and don't include viscous stresses as well as we don't add any correction owing to Laplace pressure as the interface curvature is weak. From (28), using (27), one gets

$$\frac{d^2R}{dt^2} + 4\frac{dR_l}{dt}\frac{(B-t)}{[(B-t)^2+A]} + R_l\frac{6(B-t)^2 - 2A}{[(B-t)^2+A]^2} = 0. \quad (29)$$

Equation (29) describes the linearly damped oscillatory motion of the lamella radius with time-dependent frequency and damping factor originating from the continuous transfer of momentum from the lamella to the rim. The solution for the lamella radius R_l in the $(x,y,0)$ plane is given by

$$R_l(t) = (C_1t + C_2)[(B-t)^2 + A], \quad (30)$$

with constants

$$C_1 = \frac{\upsilon(\tau_2)[(B-\tau_2)^2 + A] + 2R_{\rm jet}(\tau_2)(B-\tau_2)}{[(B-\tau_2)^2+A]^2},$$
$$C_2 = \frac{R_{\rm jet}(\tau_2)}{[(B-\tau_2)^2+A]} - C_1\tau_2 \quad (31)$$

found from the initial conditions $R_l(\tau_2) = R_{\rm jet}(\tau_2)$ and $\frac{dR_l}{dt}(\tau_2) = \upsilon(\tau_2)$ defined at the jetting stage. The maximal amplitude of the motion $R_l^{\max}$ is reached at

$$\tau_3 = \frac{2BC_1 - C_2 - \sqrt{B^2{C_1}^2 + {C_2}^2 - 3A{C_1}^2 + 2BC_1C_2}}{3C_1}. \quad (32)$$

The rim, with time going on, becomes rapidly thick compared with the lamella to which it is attached. During the expansion it is gradually fed by incoming matter from the lamella and stretched, since it borders a frontier expanding like $R_l(t)$. This leads to the semi-equilibrium value for its radius $R_{\rm rim}$ that can be easily found from (23). The volume accumulated in the rim is given by

$$\pi[R_{\rm rim}(t)]^2 2\pi R_l(t) = 2\Omega - \int_0^{R_l(t)} 2\pi r h(r,t)dr, \quad (33)$$

that with (21) and (27) gives for the rim radius

$$R_{\rm rim}(t) = \sqrt{\frac{\Omega}{\pi^2 R_l(t)} - \frac{\sigma}{2m_p\rho}\frac{[(B-t)^2+A]}{\pi R_l(t)}}. \quad (34)$$

The above equations allow calculating the rim radius at the moment of time τ_3 when the maximal amplitude is reached [Eq. (32)], corresponding to the beginning of the breakdown stage.

D. Breakdown stage

The inertia-dominated expansion stage continuously transforms into the final one that is characterized by the final formation of the prefragments and the cold breakdown of the system due to the presence of Coulomb forces. Because of the existence of the rim in the system and the quite high surface tension, the most probable physical reason for the prefragment formation seems to be the capillary instability. In this work we suggest that the instability observed is the Rayleigh-Plateau instability that causes "varicose" deformation of the rim [Fig. 4(b)]. The classical theory of the instability of and inviscid cylinder [43] suggests the dispersion relation for the perturbation amplitude coefficient A,

$$A^2 = \frac{\sigma}{R_{\rm rim}^3 m_p\rho_0}\frac{(k_fR_{\rm rim})I_1(k_fR_{\rm rim})}{I_0(k_fR_{\rm rim})}[1-(k_fR_{\rm rim})^2], \quad (35)$$

were I_0, I_1 are Bessel functions and k_f are the wave numbers. From (35) the wave number of the most unstable perturbation $k_f^{\max}$ and the associated timescale of this capillary instability,

$$k_f^{\max} \simeq \frac{0.7}{R_{\rm rim}}, \quad \tau_{\rm inst} \simeq 2.91\sqrt{\frac{m_p\rho R_{\rm rim}^3}{\sigma}}, \quad (36)$$

can be found. The values for the studied case can be obtained by inserting the rim radius from (34). That allows defining the size $\sim\frac{2\pi}{k_f^{\max}}$ and the number $\sim 0.7\frac{R_l^{\max}}{R_{\rm rim}}$ of the prefragments.

III. RESULTS AND DISCUSSION

To check the hydrodynamic approach we have chosen ^{93}Nb + ^{93}Nb system at $E = 60$ MeV/nucleon similar to the existing BUU calculations [1,2]. The surface tension coefficient is set to $\sigma = 0.972$ Mev/fm^2 [44] and the radius of the nucleus is calculated as $R = 1.3A^{\frac{1}{3}}$ fm. Evolution of the system size in the $(x,y,0)$ plane, radial particle velocity, and maximal density during the initial violent stage are shown in Figs. 5, 6, and 7. The time dependence of the jet size and average density in the origin of the jet at R_{bd} during the jetting stage is shown in Fig. 8.

The corresponding quantitative characteristics are presented in Tables III and IV. From the introduced model of the phenomena a number of qualitative and quantitative results are obtained. As mentioned earlier, within the hydrodynamic approach the difference between the soft and stiff EOS should play a major role in the first moments of the collision. From the difference in the spreading size shown in Figs. 1(c) and 1(d) and in Table IV one can see the qualitative difference between the two cases at the moment of time when the shockwave

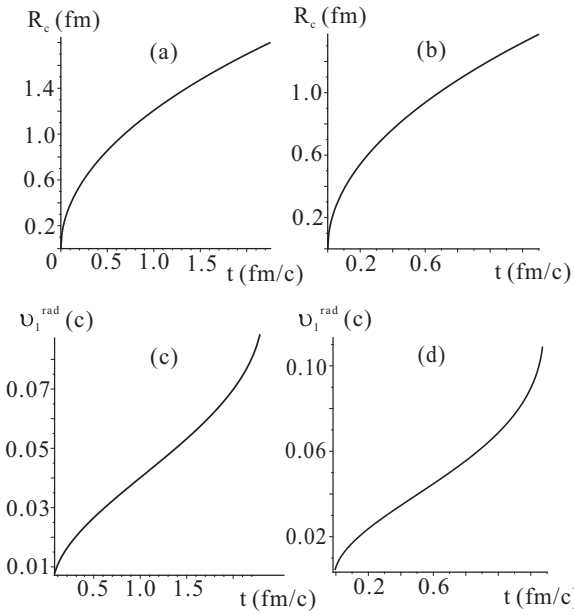

FIG. 5. Evolution of the system radius in the $(x,y,0)$ plane and radial particle velocity at the contact line during the initial violent stage. (a)–(c) Soft EOS. (b)–(d) Stiff EOS.

reaches the free boundary of the nucleus. This leads to different mechanisms being involved in the system evolution. In the case of "soft" EOS the shockwave produced on impact can be reflected from the free boundary and focused on the symmetry axis of the system [1,14,24]. This may result in rarefaction with the cavity formation along the axis, followed by bubble entrapment due to cavity collapse that will lead to the bubble geometry. In the case of stif EOS the system looks like an expanding pancake. The reflected shockwave will not play that important role, but one will instead observe

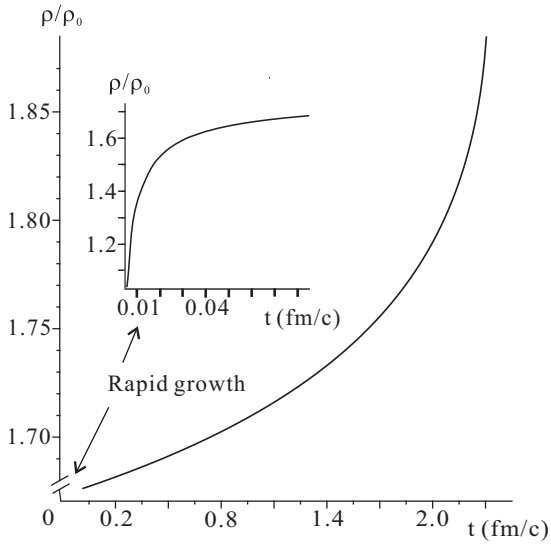

FIG. 6. Time dependence of the system density at thw contact point for the case of soft EOS. The insert shows the rapid growth of the density during the very early moments of the collision.

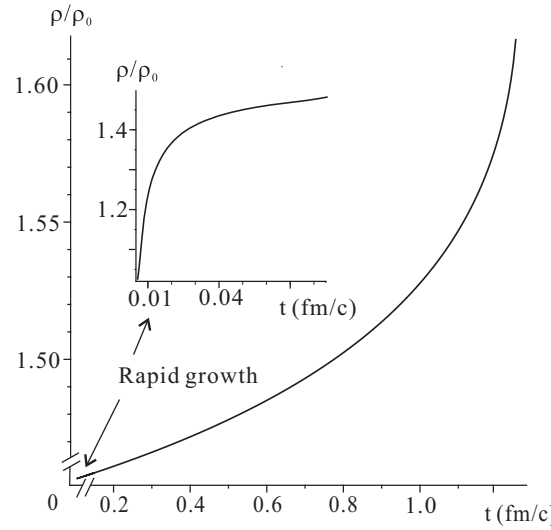

FIG. 7. Time dependence of the system density at the contact point for the case of stiff EOS. The inset shows the rapid growth of the density during the very early moments of the collision.

the inertia-dominated expansion of a pancake that has much in common with the problem of an expanding liquid sheet [45]. Therefore, one can see that the topological properties of the system are defined during the first stages of the collision.

It is important to mention several effects that do not correspond well to the picture observed in the BUU calculations [1]: first, the rapid growth of the system density (Figs. 6 and 7), and second, a very short timescale of the initial violent stage (Table III). We suggest that these discrepancies come from two approximations of the introduced model. First, the density is assumed to be uniform in the nucleus, thus the realistic density distribution [46] is not included in our calculations. Accounting for that difference can change the results for the reaction time and the slope of the density growth in the system. Second is the nature of the hydrodynamic description. In the first moments of the reaction only few particles participate in the process. In the hydrodynamic approach we have a continuous function from the very beginning that can lead to problems capturing the exact picture when the number of

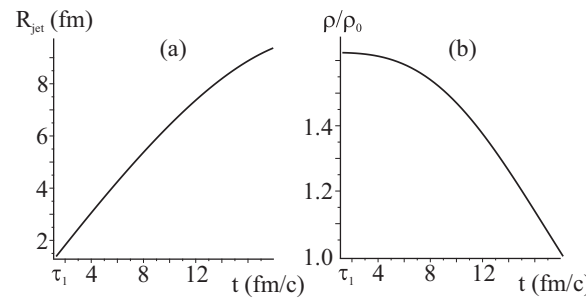

FIG. 8. Time dependence of the (a) jet size at the origin of the jet in the $(x,y,0)$ plane and (b) average density in the jet cross section at its origin during the jetting stage for the case of stif EOS.

TABLE III. Quantitative characteristics of the initial violent stage. The ^{93}Nb + ^{93}Nb system at 60 MeV/nucleon in the cases of soft ($K = 200$ MeV) and stiff ($K = 380$ MeV) EOS.

	Soft EOS	Stiff EOS
Timescale τ_1 (fm/c)	2.3	1.3
Particle radial velocity υ_1^{rad} (c)	0.09	0.11
Spreading size R_c (fm)	1.8	1.4
Shape change, $\Delta D/D$	0.024	0.014
Maximum density, ρ/ρ_0	1.9	1.6
Maximum Pressure P_1 (MeV/fm^3)	8.5	11.6

the reaction participants in the real system is small. Still, we think that the qualitative picture obtained within the introduced model is correct and the obtained maximum values represent a realistic picture of the process. At the same time a detailed analysis of the density distribution in real nucleus and its influence on the initial stage timescales is needed in order to obtain completely reliable results that are to be presented elsewhere [35].

The system evolution during the expansion and breakdown stages is investigated for the case of stiff EOS ($K = 380$ MeV). The lamella radius evolution with time during the expansion stage is shown in Fig. 9. The main quantitative estimations and their comparison with the BUU calculations and experimental data are presented in Table V.

One can see that the suggested model slightly overestimates the spreading size and underestimates the reaction time. We suggest that it comes from the approximations used in the model. For example, accounting for the viscous dissipation and changes in the Navier-Stokes equations as well as accounting for changes in the surface tension coefficient due to the temperature increase can influence both of the above values. Among the other possibilities to improve the agreement are accounting for the density distribution within the nucleus, which can influence the timescale of the initial stage, and employing different models for the jet shapes in the first stages of the process. Obtaining precise results requires detailed analysis of the influence of the employed approximations on system behavior and will be presented elsewhere [35]. We do not claim our model, as it is, gives strict results. We rather believe it to give as clear a picture as possible of the involved physical processes. Therefore, we tried to build an approximate model allowing for the analytical solutions at each stage that can be helpful in understanding the underlying physical mechanisms of the phenomena. For such a model with no adjustable parameters the results for the maximum density and

TABLE IV. Quantitative characteristics of the jetting stage; ^{93}Nb + ^{93}Nb system at 60 MeV/nucleon in the cases of soft ($K = 200$ MeV) and stiff ($K = 380$ MeV) EOS.

	Soft EOS	Stif EOS
Timescale τ_2 (fm/c)	23	18
Spreading size, R_{jet}/R	1.2	1.6
Shape change, $\Delta D/D$	0.25	0.19

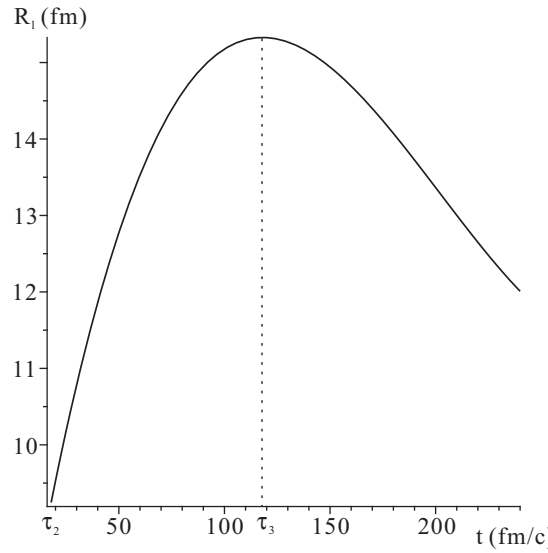

FIG. 9. Lamella radius dependence on time in the $(x,y,0)$ plane; ^{93}Nb + ^{93}Nb system at 60 MeV/nucleon with stif EOS ($K = 380$ MeV).

overall timescale of the process are in a good correspondence with the BUU calculations. It is also worth mentioning that the result for the number of fragments of similar mass is in a good correspondence both with the experiment and the BUU calculations. However, this agreement is not fully clear since the surface terms are not explicitly included in the BUU calculations [1].

The question that may arise is the growth time of the Rayleigh-Plateau instability, which is $\tau_{\text{break}} \simeq 97$ fm/c for our case. That is smaller than the maximum expansion time $\tau_3 \sim 118$ fm/c and within the typical timescale of the fragment formation in central HIC at about 50–100 MeV/nucleon; that is, 100–200 fm/c [47]. At the same time, taking into account the decrease of the surface tension coefficient with temperature towards zero at the critical temperature [48] will make the situation worse, even though the thermal excitation energies are low enough at the concerned reactions, E_{thermal}/nucleon ∼1–2 MeV [2]. Still, we suggest that the above instability can lead to the system breakdown. The main idea is that it is only one part of the mechanism that causes the formation of the prefragments and defines their sizes, when the final fragmentation occurs due to the presence

TABLE V. Quantitative characteristics of the process for the ^{93}Nb + ^{93}Nb system at 60 MeV/nucleon with stif EOS ($K = 380$ MeV).

	This work	[1,2]	[5]
Reaction time τ_3 (fm/c)	118	120–160	
Maximum density, ρ/ρ_0	1.6	∼1.5	
Spreading size, $\frac{R_i^{\max}}{R}$	2.6	∼2	
Rim radius at τ_3 (fm)	1.9		
Number of similar mass IMFs	5.6	3–6	4–6

of the Coulomb forces that make the fragments tear apart. Therefore, to give the final answer about the possibility of the realization of the suggested mechanism, precise quantitative analysis of the role of Coulomb forces and estimates of the viscosity influence are needed. At this point we would like to recall the other possible rim instabilities that can cause the fragments formation different from Rayleigh-Plateau. In some works [1,49] the Rayleigh-Taylor mechanism was suggested to be responsible for fragment formation. From our results it seems to be questionable. We have calculated the minimum wavelength of the unstable perturbations in the rim with the parameters obtained within our model. It resulted in $\lambda_{\text{inst}} \approx 70$ fm when the length of the rim is $l_{\text{rim}} \approx 96$ fm. The above values show that the Rayleigh-Taylor instability cannot explain the number of fragments.

In the suggested explanation an important part is formation of the rim during the expansion stage. Even though such a picture was not reported in the available numerical simulation of the head-on HIC, the presence of the rim does not contradict the presented density distributions (e.g., Figs. 13 and 14 from Ref. [6]).

We would also like to mention another possible mechanisms of the discussed phenomena. Spinodal decomposition seems to be quite attractive as instability develops within quite short period of time $\tau \sim 50$ fm/c and is quite sensitive to the nuclear incompressibility [50]. The main concern is the size of the system [11] as the prefragment formation occurs already in hollow structures as can be seen from the BUU calculations [2,6]. Hence, the system is about several fermis. At the same time, it is unstable only to perturbations with quite big wavelength [51]. Even though quite a lot was done to study the influence of the finite-size effects on the spinodal instability [52,53], it is difficult to give a straightforward answer whether or not such a mechanism can come into play in the studied systems. One of the ways to choose the correct mechanism is to study the other geometries, such as uniform systems for the different values of the impact energy or intermediate values of the incompressibility coefficient. Their occurrence as well as defining the energy range where the exotic topologies can be observed require some further studies of the possible splashing or system recoil.

To proceed with the suggested model some further studies are needed to describe the system breakdown and the influence of the Coulomb forces on this process, as in our work we only introduce the possible mechanism for the fragment formation. As for the exotic topologies it would also be very important to study the bubble geometry in detail. All this will require further investigations both from the hydrodynamic and microscopic points of view.

IV. CONCLUSIONS

In this work we try to show the possibility to obtain some new results in the studies of head-on heavy ion collisions at intermediate energies from the hydrodynamic description. The results are of more ideological value, and precise calculations will require a lot of further work. In summary, our study shows that the hydrodynamic description seems to explain the overall behavior of the system in head-on HIC in focus, and allows for a simple physical picture of the exotic structure formation. The straightforward link between the EOS and the exotic shapes of different topologies is explained. From comparison with the experimental data the stiff EOS is more favorable. The scenarios of the system evolution for the different EOS are different qualitatively rather than being the same process with different quantitative characteristics. The final shape of the system is defined at early stages of the collision and the topology is preserved up to system breakdown.

Even though our quantitative estimations are done with many approximations, they show that the suggested model with no adjusting of parameters gives the same results for the maximum density and timescales as the BUU calculations by an order of magnitude. Reasonable agreement is observed with the experimental results for the number of fragments of similar mass in the assumption of a Rayleigh-Plateau instability. Such an agreement supports the introduced model, even though it is necessary to pursue accurate considerations of the different surface effects in the nuclear matter due to the absence of a sharp surface, in order to use the suggested approach for a precise description of the head-on HIC. Obtained results allow concluding that combination of the introduced hydrodynamic approach together with the transport theory calculations can reveal the physical nature of the multifragmentation phenomena in focus, and give the possibility to proceed with extracting data on nuclear matter properties from head-on HIC at intermediate energies.

ACKNOWLEDGMENTS

This work was supported by the National Natural Science Foundation of China under Grants No. 11025524 and No. 11161130520, the National Basic Research Program of China under Grant No. 2010CB832903, and the European Commissions 7th Framework Programme (FP7-PEOPLE-2010-IRSES) under Grant Agreement Project No. 269131.

[1] W. Bauer, G. F. Bertsch, and H. Schulz, Phys. Rev. Lett. **69**, 1888 (1992).
[2] H. M. Xu, J. B. Natowitz, C. A. Gagliardi, R. E. Tribble, C. Y. Wong, and W. G. Lynch, Phys. Rev. C **48**, 933 (1993).
[3] C.-Y. Wong, Phys. Rev. Lett. **55**, 1973 (1985).
[4] L. G. Moretto, K. Tso, and G. J. Wozniak, Phys. Rev. Lett. **78**, 824 (1997).
[5] N. T. B. Stone, O. Bjarki, E. E. Gualtieri, S. A. Hannuschke, R. Lacey, J. Lauret, W. J. Llope, D. J. Magestro, R. Pak, A. M. Vander Molen, G. D. Westfall, and J. Yee, Phys. Rev. Lett. **78**, 2084 (1997).
[6] L. W. Chen, V. Greco, C. M. Ko, and B. A. Li, Phys. Rev. C **68**, 014605 (2003).
[7] G. Bertsch and S. D. Gupta, Phys. Rep. **160**, 189 (1988); Y. Abe, S. Ayik, P.-G. Reinhard, and E. Suraud, *ibid.* **275**, 49 (1996); V. Baran, M. Colonna, V. Greco, and M. D. Toro, *ibid.* **410**, 335 (2005); B.-A. Li, L.-W. Chen, and C. M. Ko, *ibid.* **464**, 113 (2008).

[8] P. J. Siemens and J. O. Rasmussen, Phys. Rev. Lett. **42**, 880 (1979); H. Stocker, R. Cusson, J. Maruhn, and W. Greiner, Z. Phys. A **294**, 125 (1980).
[9] H. Baumgardt, J. U. Schott, Y. Sakamoto, E. Schopper, H. Stocker, J. Hofmann, W. Scheid, and W. Greiner, Z. Phys. A **273**, 359 (1975).
[10] P. Huovinen and P. V. Ruuskanen, Annu. Rev. Nucl. Part. Sci. **56**, 163 (2006).
[11] K. V. Cherevko, L. A. Bulavin, and V. M. Sysoev, Phys. Rev. C **84**, 044603 (2011).
[12] G. Lagubeau, M. A. Fontelos, C. Josserand, A. Maurel, V. Pagneux, and P. Petitjeans, J. Fluid Mech. **713**, 50 (2012).
[13] C. Fuchs and H. Wolter, Eur. Phys. J. A **30**, 5 (2006); F.-S. Zhang and E. Suraud, Phys. Lett. B **319**, 35 (1993); Phys. Rev. C **51**, 3201 (1995).
[14] D. Bartolo, C. Josserand, and D. Bonn, Phys. Rev. Lett. **96**, 124501 (2006).
[15] R. Rioboo, M. Marengo, and C. Tropea, Exp. Fluids **33**, 112 (2002).
[16] S. T. Thoroddsen and J. Sakakibara, Phys. Fluids **10**, 1359 (1998).
[17] K.-L. Pan, P.-C. Chou, and Y.-J. Tseng, Phys. Rev. E **80**, 036301 (2009).
[18] G. Q. Li and R. Machleidt, Phys. Rev. C **48**, 1702 (1993); T. Alm, G. Ropke, W. Bauer, F. Daffin, and M. Schmidt, Nucl. Phys. A **587**, 815 (1995); Q. Li, Z. Li, S. Soff, M. Bleicher, and H. Stocker, J. Phys. G: Nucl. Part. Phys. **32**, 407 (2006).
[19] H. H. K. Tang and C.-Y. Wong, Phys. Rev. C **21**, 1846 (1980).
[20] R. D. Schroll, C. Josserand, S. Zaleski, and W. W. Zhang, Phys. Rev. Lett. **104**, 034504 (2010).
[21] J. de Ruiter, R. E. Pepper, and H. A. Stone, Phys. Fluids **22**, 022104 (2010).
[22] G. Lagubeau, M. A. Fontelos, C. Josserand, A. Maurel, V. Pagneux, and P. Petitjeans, J. Fluid Mech. **713**, 50 (2012).
[23] H. Stocker and W. Greiner, Phys. Rep. **137**, 277 (1986).
[24] J. Eggers, M. A. Fontelos, C. Josserand, and S. Zaleski, Phys. Fluids **22**, 062101 (2010).
[25] A. V. Chizhov and A. A. Shmidt, J. Tech. Phys. **45**, 18 (2000).
[26] I. V. Roisman, C. Planchette, E. Lorenceau, and G. Brenn, J. Fluid Mech. **690**, 512 (2012).
[27] F. J. Heymann, J. Appl. Phys. **40**, 5113 (1969).
[28] M. B. Lesser, Proc. R. Soc. London A **377**, 289 (1981).
[29] F.-S. Zhang, Z. Phys. A **356**, 163 (1996); F.-S. Zhang and L. X. Ge, *Nuclear Multifragmentation* (Science Press, Beijing, 1998).
[30] K. K. Haller, D. Poulikakos, Y. Ventikos, and P. Monkewitz, J. Fluid Mech. **490**, 1 (2003).
[31] A. L. Ruoff, J. Appl. Phys. **38**, 4976 (1967).
[32] N. N. Pashkov and F. M. Dolgachev, *Hydraulics. Fundamentals of Hydrology* (Energoatomizdat, Moscow, 1985).
[33] S. S. Kutateladze and M. A. Styrikovich, *Hydrodynamics of Gas-Liquid Systems* (Energy Publishers, Moscow, 1976).
[34] A. A. Korobkin, Philos. Trans. R. Soc. London A **355**, 507 (1997).
[35] K. Cherevko, J. Su, L. A. Bulavin, V. M. Sysoev, and F.-S. Zhang (unpublished).
[36] K. K. Haller, Y. Ventikos, and D. Poulikakos, J. Appl. Phys. **92**, 2821 (2002).
[37] K. Cherevko, J. Su, L. A. Bulavin, V. M. Sysoev, and F.-S. Zhang, Nucl. Sci. Technol. **24**, 050515 (2013).
[38] Y. Pan and K. Suga, Phys. Fluids **17**, 082105 (2005).
[39] P. Zhang and C. K. Law, Phys. Fluids **23**, 042102 (2011).
[40] J. E. Field, J. P. Dear, and J. E. Ogren, J. Appl. Phys. **65**, 533 (1989).
[41] E. Villermaux and B. Bossa, J. Fluid Mech. **668**, 412 (2011).
[42] E. Villermaux and C. Clanet, J. Fluid Mech. **462**, 341 (2002).
[43] S. Chandrasekhar, *Hydrodynamic and Hydromagnetic Instability* (Dover, New York, 1961).
[44] D. Ravenhall, C. Pethick, and J. Lattimer, Nucl. Phys. A **407**, 571 (1983).
[45] A. I. Fedorchenko, A.-B. Wang, and Y.-H. Wang, Phys. Fluids **17**, 093104 (2005).
[46] M. Brack, C Guet, and H.-B. Hakansson, Phys. Rep. **123**, 275 (1985).
[47] J. Aichelin, Phys. Rep. **202**, 233 (1991).
[48] A. D. Panagiotou, M. W. Curtin, H. Toki, D. K. Scott, and P. J. Siemens, Phys. Rev. Lett. **52**, 496 (1984).
[49] R. Allen, J. Colloid Interface Sci. **51**, 350 (1975).
[50] A. B. Larionov and I. N. Mishustin, Phys. At. Nucl. **57**, 636 (1994).
[51] J. W. Cahn, J. Chem. Phys. **42**, 93 (1965).
[52] B. Jacquot, S. Ayik, Ph. Chomaz, and M. Colonna, Phys. Lett. B **383**, 247 (1996).
[53] Ph. Chomaz, M. Colonna, and J. Randrup, Phys. Rep. **389**, 263 (2004).